Proceedings of the Thirteenth International Conference on
Engineering Computational Technology
Edited by: P. Iványi, J. Kruis and B.H.V. Topping
Civil-Comp Conferences, Volume 13, Paper 2.3
Civil-Comp Press, Edinburgh, United Kingdom, 2026
ISSN: 2753-3239, doi: 10.4203/ccc.13.2.3

Ellipsoidal Kinematic Reconstruction for the Neighborhood Deformation Tracking in Nonlocal Analyses

S. Kim[1], S. Jin[2] and J.-W. Hong[1]

[1] Civil and Environmental Engineering, KAIST, Republic of Korea
[2] Department of Mechanical Engineering, Pukyong National University, Republic of Korea

Abstract

Nonlocal methods such as peridynamics are effective for the analysis of large deformations, yet the simplification of the geometric evolution of the neighborhood often leads to physical inconsistencies. In this study, an ellipsoidal kinematic reconstruction method is proposed to accurately capture the changes in the shape and volume of the neighboring area of each node. The proposed method identifies specific marker nodes along the initial Cartesian axes and decouples the rigid body rotation from the stretching of the support domain through a hierarchical rotation decomposition. This alignment provides a stable basis for an ellipsoidal mapping to quantify the stretch ratios and the change of the nodal volume. To verify the accuracy of the rotation and volume tracking, rigid body rotation and axial stretching tests are performed. The results demonstrate the precise recovery of rotation angles and the local volume ratio even under significant nodal irregularity, confirming the robustness and coordinate invariance of the framework. Consequently, the ellipsoidal kinematic reconstruction method establishes a reliable kinematic foundation for nonlocal models. This method is applicable to the thermomechanical analysis of peridynamics to ensure physical consistency and stability under large deformations.

Keywords: nonlocal method, large deformation, peridynamics, thermomechanics, heat conduction, ellipsoidal mapping

1 Introduction

The occurrence of large deformations are common in many engineering applications, such as high-velocity impacts, metal forming, and structural failure under extreme loads. Accurately predicting these phenomena is an important challenge. The traditional mesh-based finite element method (FEM) has been used for these analyses, but it often suffers from severe mesh distortion, element entanglement, and numerical instabilities. These issues require computationally expensive remeshing or complex stabilization schemes. To circumvent these geometric constraints, various nonlocal methods have been developed, offering a more flexible description of material behavior without the need for fixed topological connectivity.

Peridynamics (PD), a nonlocal continuum theory, was introduced as an alternative to conventional mesh-based approaches to overcome the difficulties of handling discontinuities and large deformations [1,2]. By replacing spatial derivatives with integral expressions, PD avoids the need for predefined meshes and naturally accommodates features such as cracks and interfaces without special treatment. In this framework, the mechanical response of a point is determined by integrating interactions within a finite neighborhood known as the horizon [3–7]. This nonlocal nature allows for a natural description of complex failure modes and multi-physical coupling, such as the thermomechanical evolution often encountered in extreme environments.

However, ensuring the physical consistency of nonlocal models under large deformations remains a critical challenge. Most existing peridynamic formulations assume that the horizon remains undistorted or that the nodal volume stays constant at its initial value throughout the simulation. While these simplifications are computationally efficient, they can introduce significant numerical errors during substantial stretching or rotation. Specifically, failing to update the geometric evolution of the neighborhood leads to an inaccurate representation of weight functions, local volume changes, and the resulting constitutive response.

To address these limitations, this study introduces an ellipsoidal kinematic reconstruction (EKR) framework to track the local kinematic state. The procedure begins with the selection of specific marker nodes that serve as anchors for tracking the motion of the neighborhood. For nodes at material boundaries, a symmetric extension scheme is applied to compensate for truncated horizons by mirroring available marker data. Then, the local rotation is decoupled through a two-step hierarchical decomposition process to establish a local reference frame. Based on this reconstructed frame, the deformed neighborhood is modeled as an evolving ellipsoid, which is used to calculate the stretch ratios and the local Jacobian of each node.

To verify the accuracy and robustness of the EKR framework, a series of numerical tests is conducted. These include rigid-body rotation tests and uniaxial stretching tests under various conditions. The performance of the method is analyzed for both regular and irregular nodal distributions, as well as for nodes located at the interior and the boundaries of the domain.

2 Theoretical Background and Motivation

2.1 Thermomechanical Formulations in Peridynamics

In peridynamics, a physical quantity at a node is evaluated by integrating the contributions of its neighboring nodes within a distance, called horizon. For a node at position $\mathbf{x}$, the set of its neighboring nodes within the horizon is denoted by $H_x = \{\mathbf{x}' | \, \|\mathbf{x}' - \mathbf{x}\| \leq \delta\}$. Peridynamics is widely applied to thermomechanical problems.

In this framework, the equation of motion representing the mechanical behavior can be expressed in the peridynamics equation as [4]

$$\rho \ddot{\mathbf{u}} (\mathbf{x}, t) = \int_{H_x} \mathbf{f} \left(\mathbf{u} (\mathbf{x}', t) - \mathbf{u} (\mathbf{x}, t) , \mathbf{x}' - \mathbf{x} \right) \mathrm{d}V' + \mathbf{b} (\mathbf{x}, t) , \tag{1}$$

where ρ is the density, $\mathbf{u}$ is the displacement vector, $\mathbf{f}$ is the pairwise force vector, $\mathrm{d}V'$ is the volume occupied by $\mathbf{x}'$, and $\mathbf{b}$ is the body force density. Similarly, the heat diffusion equation can be written as [8]

$$\rho c_v \dot{\Theta}(\mathbf{x}, t) = \int_{H_x} \left(q(\mathbf{x}, \mathbf{x}', t) + \Theta(\mathbf{x}, t) \beta(\mathbf{x}' - \mathbf{x}) \dot{e}(\mathbf{x}' - \mathbf{x}) \right) \mathrm{d}V' + h^B (\mathbf{x}, t) , \tag{2}$$

where c_v is the volumetric specific heat, Θ is the temperature, and q represents the heat flow density through the virtual thermal bond. The term β denotes the peridynamic thermal modulus, $\dot{e}$ is the rate of change of bond extension, and h^B is the heat generation rate per unit volume. By neglecting the mechanical coupling term involving the bond extension rate in Eq. (2), the formulation can be simplified for pure heat conduction analysis [9]. For instance, Figure 1 shows the results of a heat conduction analysis for a manifold geometry with complex internal channels. Furthermore, these governing equations enable fully coupled thermomechanical analyses, such as the thermal expansion shown in Figure 2.

2.2 Limitations in Large Deformation Analyses

In the numerical implementation of these formulations, weight functions $w(\|\mathbf{x}' - \mathbf{x}\|)$ are often introduced to account for the decaying influence of neighbors with distance [10]. In many existing models, this weight function is defined only based on

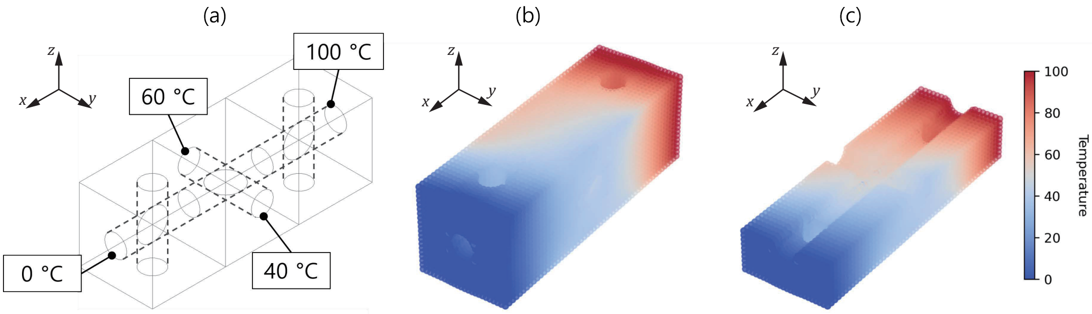

Figure 1: Heat conduction analysis on a manifold geometry using peridynamics: (a) geometry and temperature boundary conditions of the analysis, (b) the temperature distribution of nodes, and (c) the internal cross-section view.

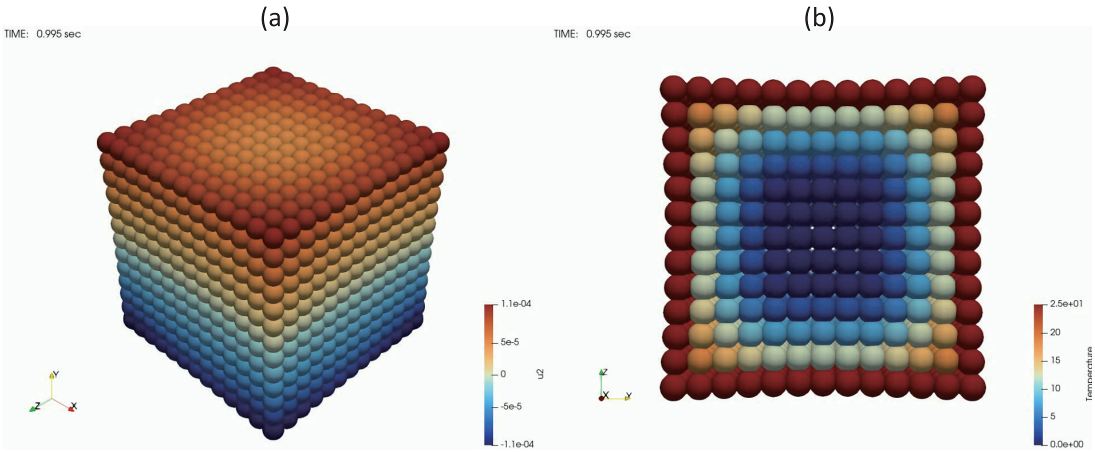

Figure 2: Thermal expansion analysis using peridynamics: (a) y-directional displacements and (b) the temperature distribution of nodes.

the initial distance in the reference configuration. Furthermore, the nodal volume $\mathrm{d}V'$ used in the integration is typically assumed to remain constant at its initial value. Isotropic domain and constant volume assumptions are suitable for small strains but become physically inconsistent under large deformations. Therefore, reflecting such changes in the weight functions and nodal volumes is necessary.

3 Ellipsoidal Kinematic Reconstruction

In this study, an ellipsoidal kinematic reconstruction (EKR) method is proposed to accurately capture the geometric evolution of the neighborhood under large deformations. The framework consists of the identification of marker nodes, a hierarchical rotation decomposition for the alignment of the local axes, and an ellipsoidal mapping for the estimation of the stretch ratios and the change of the nodal volume. By decoupling the rigid body rotation from the stretching of the support domain, the EKR ensures that the deformation is measured independently of the coordinate frame. A schematic of the overall EKR procedure is presented in Figure 3.

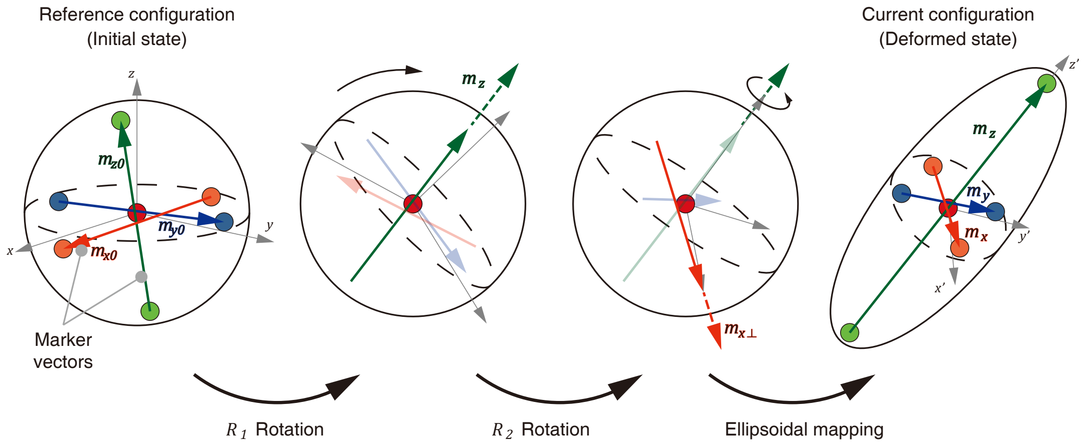

Figure 3: Schematic of the ellipsoidal kinematic reconstruction (EKR) procedure.

3.1 Marker-node Selection and Vector Construction

The procedure begins with the identification of specific marker nodes within the horizon H_x of a node $\mathbf{x}$ at the initial reference configuration. In three-dimensional space, up to six markers—denoted as $\mathbf{x}'_{x\pm}$, $\mathbf{x}'_{y\pm}$, and $\mathbf{x}'_{z\pm}$—are selected as the extreme points along the initial Cartesian axes. These points serve as a discrete representation of the boundary of the horizon and define its deformed shape. Even under irregular nodal distributions, this selection ensures that the markers capture the maximum extent of the domain in each coordinate direction.

Following the identification of the marker nodes, three marker vectors denoted as $\mathbf{m}_{x0}$, $\mathbf{m}_{y0}$ and $\mathbf{m}_{z0}$ are constructed. For an interior node where all marker pairs are available, these vectors are defined by the relative positions of the positive and negative markers as

$$\mathbf{m}_{[\cdot]0} = \mathbf{x}'_{[\cdot]+} - \mathbf{x}'_{[\cdot]-}, \tag{3}$$

where $[\cdot]$ denotes the $x, y,$ or z axis. These vectors provide the basis for the next procedure of EKR. At the boundary of the material, the horizon is often truncated, which results in missing marker nodes. A symmetric extension is applied to maintain the consistency of the marker vectors. If only one marker of a pair is available, the marker vector is determined by doubling the relative displacement of the available marker from the position of the central node as

$$\mathbf{m}_{[\cdot]0} = \begin{cases} 2(\mathbf{x}'_{[\cdot]+} - \mathbf{x}) & \text{if } \mathbf{x}'_{[\cdot]-} \text{ is missing,} \\ 2(\mathbf{x} - \mathbf{x}'_{[\cdot]-}) & \text{if } \mathbf{x}'_{[\cdot]+} \text{ is missing.} \end{cases} \tag{4}$$

This restoration prevents bias in the geometric representation and ensures a stable volume estimation at the edges of the domain.

3.2 Hierarchical Rotation Decomposition Algorithm

The positions of the marker nodes change from $\mathbf{x}'_{[\cdot]\pm}$ in the reference configuration to $\mathbf{y}'_{[\cdot]\pm}$ in the deformed current configuration. The marker vector in the current configuration is defined as

$$\mathbf{m}_{[\cdot]} = \mathbf{y}'_{[\cdot]+} - \mathbf{y}'_{[\cdot]-}. \tag{5}$$

The evolution of the horizon is tracked based on the change of these marker vectors. The rotation of the horizon is decoupled from the deformation through two sequential rotations, designated as swing (R_1) and twist (R_2).

To ensure coordinate invariance, the anchor vector for the swing rotation is not fixed to a specific global axis. Instead, the marker vector with the most significant angular deviation is selected to provide numerical stability. The unit vectors of the initial and current marker vectors are given by

$$\mathbf{a}_{[\cdot]} = \frac{\mathbf{m}_{[\cdot]0}}{\|\mathbf{m}_{[\cdot]0}\|}, \quad \mathbf{b}_{[\cdot]} = \frac{\mathbf{m}_{[\cdot]}}{\|\mathbf{m}_{[\cdot]}\|}. \tag{6}$$

The cosine of the angular deviation for each axis is determined through the inner product as

$$\cos\theta_{[\cdot]} = \mathbf{a}_{[\cdot]} \cdot \mathbf{b}_{[\cdot]} \tag{7}$$

The primary anchor index k is determined where $\cos\theta_k$ is the minimum value among all axes. The rotation matrix $\mathbf{R}_1$ is then constructed using the cross product $\mathbf{v} = \mathbf{a}_k \times \mathbf{b}_k$ and the dot product $c = \mathbf{a}_k \cdot \mathbf{b}_k$ according to the Rodrigues' rotation formula as [11]

$$\mathbf{R}_1 = \mathbf{I} + \mathbf{V}_\times + \frac{1}{1+c}\mathbf{V}_\times^2, \tag{8}$$

where $\mathbf{V}_\times$ is the skew-symmetric matrix of $\mathbf{v} = [v_x, v_y, v_z]$, defined as

$$\mathbf{V}_\times = \begin{bmatrix} 0 & -v_z & v_y \\ v_z & 0 & -v_x \\ -v_y & v_x & 0 \end{bmatrix}. \tag{9}$$

To determine the subsequent twist rotation (R_2), the current marker vectors are transformed using the transpose of $\mathbf{R}_1$. The transformed marker vectors $\mathbf{m}^{(1)}_{[\cdot]}$ are obtained as

$$\mathbf{m}^{(1)}_{[\cdot]} = \mathbf{R}_1^{\mathrm{T}}\mathbf{m}_{[\cdot]}. \tag{10}$$

After this transformation, the transformed primary anchor vector $\mathbf{m}^{(1)}_k$ is parallel to the initial vector $\mathbf{m}_{k0}$.

Following the primary alignment, a second rotation is performed to correct the torsional deviation around the aligned anchor axis. The marker vectors are projected onto the orthogonal plane defined by the initial primary anchor $\mathbf{m}_{k0}$ using the projection matrix $\mathbf{P}$, which can be calculated as

$$\mathbf{P} = \mathbf{I} - \frac{\mathbf{m}_{k0} \otimes \mathbf{m}_{k0}}{\mathbf{m}_{k0}^{\mathrm{T}} \mathbf{m}_{k0}} = \mathbf{I} - \frac{\mathbf{m}_{k0} \mathbf{m}_{k0}^{\mathrm{T}}}{\mathbf{m}_{k0}^{\mathrm{T}} \mathbf{m}_{k0}}. \tag{11}$$

For the remaining directions j and l, the planar projections of the initial marker vectors and the transformed marker vectors can be obtained as

$$\mathbf{m}_{[\cdot]0\perp} = \mathbf{P}\mathbf{m}_{[\cdot]0}, \quad \mathbf{m}_{[\cdot]\perp}^{(1)} = \mathbf{P}\mathbf{m}_{[\cdot]}^{(1)}, \tag{12}$$

where $[\cdot]$ denotes the secondary indices j and l, and the vectors $\mathbf{m}_{[\cdot]0\perp}$ and $\mathbf{m}_{[\cdot]\perp}^{(1)}$ are the projected vectors.

By projecting these vectors, The components parallel to the primary axis are eliminated, allowing for a pure rotational comparison. The angular difference in the projected plane can be quantified through the inner product as

$$\cos\theta_{[\cdot]\perp} = \frac{\mathbf{m}_{[\cdot]0\perp} \cdot \mathbf{m}_{[\cdot]\perp}^{(1)}}{\|\mathbf{m}_{[\cdot]0\perp}\| \|\mathbf{m}_{[\cdot]\perp}^{(1)}\|}. \tag{13}$$

A secondary anchor j is identified by selecting the marker with the largest angular deviation in the projected plane. The twist rotation matrix $\mathbf{R}_2$ is then defined to align $\mathbf{m}_{j0\perp}$ with $\mathbf{m}_{j\perp}^{(1)}$ around the initial primary axis $\mathbf{a}_k$. The composite rotation matrix $\mathbf{R}$ that maps the reference configuration to the current configuration is obtained as

$$\mathbf{R} = \mathbf{R}_1 \mathbf{R}_2. \tag{14}$$

The resulting rotated frame provides the foundation for the ellipsoidal mapping.

3.3 Ellipsoidal Mapping

The geometric change of the horizon is modeled as an ellipsoid based on the rotation matrix $\mathbf{R}$. The principal axes of the ellipsoid are defined by the column vectors of $\mathbf{R}$, denoted as $\mathbf{r}_x$, $\mathbf{r}_y$, and $\mathbf{r}_z$. To quantify the deformation, the stretch ratio $a_{[\cdot]}$ along each principal axis is determined by comparing the projections of the marker vectors onto the corresponding axes in both configurations as

$$a_{[\cdot]} = \frac{\mathbf{m}_{[\cdot]} \cdot \mathbf{r}_{[\cdot]}}{\mathbf{m}_{[\cdot]0} \cdot \mathbf{e}_{[\cdot]}}, \tag{15}$$

where $\mathbf{e}_{[\cdot]}$ represents the unit basis vector of the reference configuration. This projection-based approach isolates the pure deformation along each principal direction, even if the initial positions of the markers are not aligned with the Cartesian axes.

The change in the local volume can be determined through the determinant of the Jacobian matrix $\mathbf{J}$ at the node. Under the assumption of a linear ellipsoidal expansion along the local principal axes, the Jacobian matrix simplifies to a diagonal matrix with the stretch ratios as diagonal elements. The local volume ratio J can be calculated as

$$J = \frac{\mathrm{d}V}{\mathrm{d}V_0} = |\det(\mathbf{J})| = a_x a_y a_z \tag{16}$$

where $\mathrm{d}V_0$ and $\mathrm{d}V$ represent the nodal volumes in the reference and current configurations, respectively.

Furthermore, the weight function w is updated to account for the ellipsoidal deformation of the horizon through an effective distance d_{eff}. For a relative displacement vector $\boldsymbol{\eta}$ between the central node and a neighbor node in the current configuration, d_{eff} is defined by mapping the ellipsoidal coordinates back to the reference spherical domain as

$$d_{\text{eff}} = \sqrt{\left(\frac{\boldsymbol{\eta}\cdot\mathbf{r}_x}{a_x}\right)^2 + \left(\frac{\boldsymbol{\eta}\cdot\mathbf{r}_y}{a_y}\right)^2 + \left(\frac{\boldsymbol{\eta}\cdot\mathbf{r}_z}{a_z}\right)^2}. \tag{17}$$

This effective distance scales the horizon according to the stretch ratios, ensuring that the weighting remains physically consistent under large deformations.

4 Numerical Results

To verify the accuracy and coordinate invariance of the EKR algorithm, a series of rigid body rotation tests is performed on a cube of $100 \times 100 \times 100$ mm^3. The horizon size is set to 10 mm with a uniform node spacing of 2.44 mm. The performance of the algorithm is analyzed at two observation points: the geometric center of the cube and a boundary node at the center of the $-x$ face. The symmetric extension scheme is applied to the boundary node.

To evaluate the accuracy of the rotation extraction, the cube is rotated up to $360°$ around a general axis of $(1, 1, 1)$. The recovered rotation angles show good agreement with the analytical solutions across the entire range for both interior and boundary nodes, as shown in Figure 4(a). Moreover, to verify the robustness of the algorithm, the level of nodal irregularity is incrementally increased under a fixed rotation of $30°$. The irregularity is introduced by randomly perturbing the position of each node within a range proportional to the initial nodal spacing. Even with a highly irregular nodal arrangement, the algorithm consistently identifies the exact rotation angle, as shown in Figure 4(b). This performance confirms that the dual-projection technique effectively isolates the physical rotation from the initial nodal positions regardless of the arrangement.

The performance of the framework in tracking the local volume ratio J is evaluated under large axial deformations. A bar with dimensions of $1{,}000 \times 100 \times 100$ mm^3 is subjected to uniaxial stretching in the x-direction. The lateral contraction of the bar is governed by a Poisson ratio of 0.3. The horizon size is 20 mm, and the initial nodal spacing is 4.98 mm. The local volume ratio is evaluated at the geometric center and the boundary of the bar. To verify the accuracy of the volume estimation, the axial

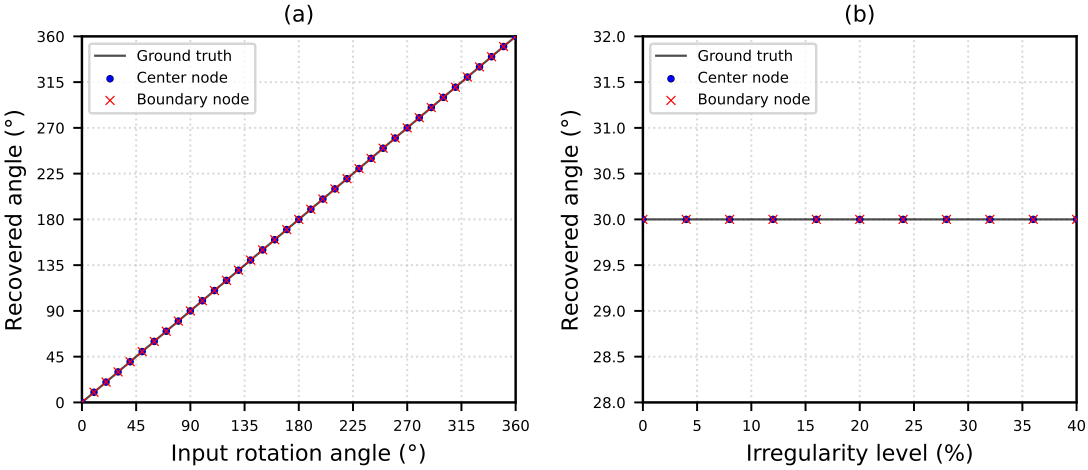

Figure 4: Rotation tracking performance: (a) accuracy across a full 360° rotation range and (b) robustness of angle recovery under varying nodal irregularity.

strain is increased for a regular nodal distribution. The ellipsoidal mapping tracks the local volume ratio, and the results show good agreement with the analytical solution even under significant stretching, as shown in Figure 5(a).

The robustness of the volume tracking is further analyzed by increasing the level of nodal irregularity under a fixed axial strain of 20%. As shown in Figure 5(b), the calculated volume ratios remain consistent with the analytical values across all levels of irregularity. The stability of these results indicates that the ellipsoidal mapping provides a reliable geometric representation independent of the nodal arrangement. Consequently, the formulation maintains physical consistency and volume conservation in nonlocal analyses under large deformations.

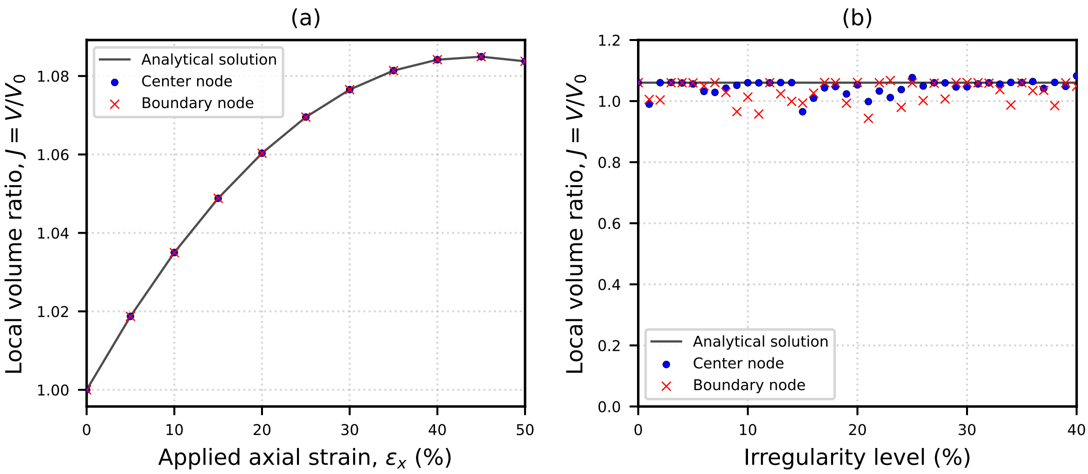

Figure 5: Volumetric deformation tracking: (a) local volume ratio under axial strain and (b) stability of volumetric tracking against varying nodal irregularity.

5 Conclusions

Nonlocal methods including peridynamics are effective for large deformations, yet the consideration of the geometric evolution of the neighborhood remains limited despite its importance for physical consistency. In this study, we propose an ellipsoidal kinematic reconstruction (EKR) to accurately capture the changes in the shape and volume of the horizon. This framework isolates the rigid body rotation from the stretching of the support domain, ensuring that the deformation is measured independently of the coordinate frame. The procedure integrates the identification of marker nodes, a hierarchical rotation decomposition (HRD), and an ellipsoidal mapping to provide a stable kinematic basis.

Specific marker nodes are identified at the extreme points along the initial Cartesian axes to provide a discrete representation of the boundary of the horizon. Based on the evolution of these markers, the HRD algorithm aligns the local coordinate axes through sequential swing and twist rotations, effectively isolating the rotation of the horizon from the total motion. The subsequent ellipsoidal mapping quantifies the stretch ratios and the change of the nodal volume along the reconstructed principal axes. This formulation enables the dynamic update of the weight functions, ensuring that the influence of neighbor nodes remains physically consistent as the geometric shape of the neighborhood evolves.

Numerical verifications demonstrate the high accuracy and robustness of the EKR. Rigid body rotation tests on a cube confirm that the algorithm perfectly recovers rotation angles up to $360°$, even under significant nodal irregularity. Furthermore, uniaxial stretching tests on a bar show that the framework accurately tracks the local volume ratio J throughout large axial deformations. The application of the symmetric extension scheme for the boundary nodes further maintains the stability of the volume estimation at truncated material boundaries.

The EKR establishes a reliable kinematic foundation for nonlocal analyses by ensuring volume conservation and objective deformation tracking. By overcoming the limitations of fixed horizons, this framework enhances the physical consistency and numerical stability of simulations under large deformations.

Acknowledgements

This work was supported by the National Research Foundation of Korea (NRF) grant funded by the Korea government (MSIT) (No. NRF-2022R1A2C2091533).

References

[1] S. Silling, E. Askari, "A meshfree method based on the peridynamic model of solid mechanics", Computers & Structures, 83(17), 1526–1535, 2005.

[2] S. Jin, J.-W. Hong, “Convergence study of stabilized non-ordinary state-based peridynamics for elastic and fracture problems”, Engineering Fracture Mechanics, 289, 109438, 2023.

[3] Liu, J.-W. Hong, “Discretized peridynamics for brittle and ductile solids”, International Journal for Numerical Methods in Engineering, 89(8), 1028–1046, 2012.

[4] W. Liu, J. W. Hong, “Discretized peridynamics for linear elastic solids”, Computational mechanics, 50, 579–590, 2012.

[5] J. Lee, J.-W. Hong, “Morphological aspects of crack growth in rock materials with various flaws”, Inter- national Journal for Numerical and Analytical Methods in Geomechanics, 43(10), 1854–1866, 2019.

[6] E. Madenci, S. Oterkus, “Ordinary state-based peridynamics for plastic deformation according to von mises yield criteria with isotropic hardening”, Journal of the Mechanics and Physics of Solids, 86, 192–219, 2016.

[7] S. Jin, Y. K. Hwang, J.-W. Hong, “Stabilized non-ordinary state-based peridynamics with irregular nodal distribution”, Mechanics Research Communications, 130, 104130, 2023.

[8] Z. Chen, F. Bobaru, “Selecting the kernel in a peridynamic formulation: A study for transient heat diffusion”, Computer Physics Communications, 197, 51–60, 2015.

[9] S. Kim, S. Jin, J.-W. Hong, “Numerical simulation of heat transfer across partial discontinuities using the peridynamic differential operator”. Computer Methods in Applied Mechanics and Engineering, 452, 118749, 2026.

[10] S. A. Silling, M. Epton, O. Weckner, J. Xu, E. Askari, “Peridynamic States and Constitutive Modeling”, Journal of Elasticity, 88(2), 151–184, 2007.

[11] L. Fraiture, “A history of the description of the three-dimensional finite rotation”. The Journal of the Astronautical Sciences, 57(1), 207-232, 2009.